Image Reconstruction from Incomplete Data

Vol. 4123

PROCEEDINGS OF SPIE
SPIE—The International Society for Optical Engineering

Image Reconstruction from Incomplete Data

Michael A. Fiddy
Rick P. Millane
Chairs/Editors

31 July–1 August 2000
San Diego, USA

Sponsored and Published by
SPIE—The International Society for Optical Engineering

Cooperating Organization
Society for Industrial and Applied Mathematics (SIAM)

Volume 4123

Please use the following format to cite material from this book:

Author(s), "Title of paper," in *Image Reconstruction from Incomplete Data*, Michael A. Fiddy, Rick P. Millane, Editors, Proceedings of SPIE Vol. 4123, page numbers (2000).

ISSN 0277-786X
ISBN 0-8194-3768-9

Published by
SPIE—The International Society for Optical Engineering
P.O. Box 10, Bellingham, Washington 98227-0010 USA
Telephone 1 360/676-3290 (Pacific Time) • Fax 1 360/647-1445
http://www.spie.org/

Printed in the United States of America.

Some of the presenters at the Conference on Image Reconstruction from Incomplete Data.

Conference Committee

Conference Chairs

Michael A. Fiddy, University of Massachusetts/Lowell (USA)
Rick P. Millane, Purdue University (USA)

Program Committee

Philip J. Bones, University of Canterbury (New Zealand)
Mark E. Brezinski, Brigham and Women's Hospital (USA) and Harvard Medical School (USA)
Charles L. Byrne, University of Massachusetts/Lowell (USA)
Julian C. Christou, Starfire Optical Range (UK)
Bruce Cornuelle, Scripps Institution of Oceanography (USA)
James R. Fienup, Veridian ERIM International, Inc. (USA)
Donald Fraser, University of New South Wales (Australia)
Haruyuki Harada, Kagoshima National College of Technology (Japan)
William Kuperman, Scripps Institution of Oceanography (USA)
Richard G. Lane, University of Canterbury (New Zealand)
Gabi Laske, Cecil H. and Ida M. Green Institute of Geophysics and Planetary Physics (USA)
Robert V. McGahan, Air Force Research Laboratory (USA)
Frank Natterer, Westfälische Wilhelms-Universität Münster (Germany)
Rocco Pierri, Seconda Università degli Studi di Napoli (Italy)
Michael B. Silevitch, Northeastern University (USA)
Thomas C. Terwilliger, Los Alamos National Laboratory (USA)
Markus E. Testorf, University of Massachusetts/Lowell (USA)

Session Chairs

1 Inverse Scattering and Radar I
Rick P. Millane, Purdue University (USA)

2 Astronomy and Imaging Through Turburlence
James R. Fienup, Veridian ERIM International, Inc. (USA)

3 Applications in Geophysics and Oceanography
Matthew Dzieciuch, Scripps Institution of Oceanography (USA)

4 Remote Sensing
Philip J. Bones, University of Canterbury (New Zealand)

5 Inverse Scattering and Radar II
Michael A. Fiddy, University of Massachusetts/Lowell (USA)

Introduction

Despite its new title, this conference is essentially a continuation of a long line of similar conferences that have been part of the mathematical imaging program for many years. A key meeting was SPIE's Applications of Mathematics in Modern Optics held in San Diego in August 1982. Our involvement with SPIE dates back to volume 413, from the Inverse Optics conference chaired by A. J. Devaney in 1983. The objective of these meetings is to bring together those working on a variety of inverse problems in a broad range of disciplines, in order to stimulate the transfer of ideas and allow a common language to evolve. Such a gathering never fails to prove stimulating and informative, even though some problems being discussed 20 years ago are still with us.

The theme of this conference was the presentation and evaluation of methods and algorithms for reconstructing signals or images from remotely sensed data. "Image" is taken here in a broad context, meaning the distribution of any physical quantity of interest which one wishes to recover from indirect data. Image reconstruction usually presents an inverse problem (e.g., "reconstructing the cow from the hamburger"), that is typically ill-posed, and presents challenging mathematical difficulties that defy analytical solutions. Such problems are usually characterized by "incomplete" data. This can be due simply to the presence of noise, but more often it is due to practical aspects such as sensor limitations that result in, for example, a limited number of data points, range of angles, range of wavelengths, missing or partial phase information, etc. The design of effective and efficient algorithms for constructing useful solutions to these kinds of problems represents a significant number of the 34 papers that were contributed to this conference. The papers were grouped into sessions focused on inverse scattering and radar, astronomy and imaging through turbulence, remote sensing, and applications in geophysics, oceanography, physics, biology, and medicine, illustrating the breadth of application of these techniques.

There were numerous excellent presentations. We would like to thank the authors and the program committee, without whose efforts this meeting would not have been so rewarding. Thanks also go to the very professional and efficient staff at SPIE for their assistance over the last year. We hope that this meeting is just one more in the ongoing sequence of conferences addressing these important and pervasive problems.

Michael A. Fiddy
Rick P. Millane

Contents

Radar Imaging Using Ultra-wideband Stochastic Waveforms

Daryl C. Bell and Ram M. Narayanan

Department of Electrical Engineering and Center for Electro-Optics,
University of Nebraska-Lincoln,
Lincoln, NE 68588-0511

ABSTRACT

The University of Nebraska-Lincoln has developed an ultra-wideband random noise radar operating over the 1-2 GHz frequency range. The system uses the technique of heterodyne correlation, and is thus phase-coherent. It has therefore been used in applications such as interferometry, polarimetry, and Doppler estimation. Recently, the system has been used for SAR and ISAR imaging of targets and terrain. This work has brought to the forefront various issues, such as the type of images obtained when utilizing a truly stochastic signal as a transmit waveform, and the techniques employed to realize this image. The natural answer to the first question is that the image obtained is based upon the expected value of the return signals, in the probabilistic sense of the word. This leads to answering the second question by determining what sort of estimators one would use to estimate this expected value. In this work, we will discuss the expected value of the image and its properties. We will then examine single look ISAR images collected in anechoic chamber experiments performed at the University of Nebraska-Lincoln.

Keywords: random noise radar, stochastic, ultra-wideband, ISAR

1. INTRODUCTION

Since the early '50s,[1] research has been conducted on the feasibility of using a noise signal, or random signals, as a transmit signal for a radar. These radars have been used for the measurement of range profiles,[2] Doppler estimation,[3] the detection of buried objects,[4] interferometry,[5] and ISAR and SAR imaging.[6–8] This list is far from complete and does not reflect the extent of the literature on noise radars. For a more complete listing, we refer the reader to *Guosui et. al.*.[9] Most of the preceding work, although based on a theoretical concept, is actual experimental verification of the usefulness of such radars. The theoretical analysis of random signal imaging is much less extensive. To cite a few examples we have the early work of *Grant et. al.*,[10] the measurement of radar cross-section and calibration of these systems,[11] and the calculation of an "average ambiguity function" and characterization of the radar returns in *Guosui et. al.*[9] and the references therein. We are specifically interested in radar imaging.[12] To this end, we wish to lay a somewhat general theoretical foundation for radar imaging utilizing truly random processes. By "general", we will not restrict ourselves to the assumption of a narrow-band process. In fact, we are quite interested in ultra-wideband radar and their usefulness in ISAR and SAR imaging. We intend to establish the foundation to assist in understanding the advantages and limitations of using a random signal radar system for radar imaging.

In this paper, we calculate the point-spread functions of a 1- and 2-dimensional radar imaging systems by considering them as the expected value of the radar return. Also, under the assumption that we have real valued Gaussian processes, we compute the variances of the returns. However, Doppler measurement presumes that the radar is phase-coherent. We also present a series of turntable experiments utilizing this unique radar system that clearly underscore its ability to yield high resolution ISAR images. In these experiments, we examine the cross-range resolution of the ultra-wideband system, the variation of single look images, and we present polarimetric images of a complex target.

Dr. Bell's E-mail: dbell@unlserve.unl.edu, Dr. Narayanan's E-mail: rmarayanan@unl.edu

Image Reconstruction from Incomplete Data, Michael A. Fiddy, Rick P. Millane, Editors,
Proceedings of SPIE Vol. 4123 (2000) © 2000 SPIE. · 0277-786X/00/$15.00

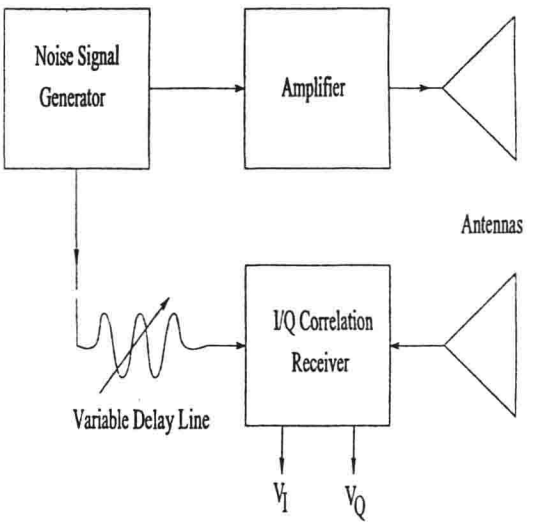

Figure 1. Block diagram of ultra-wideband polarimetric random noise radar system.

2. THEORETICAL CONSIDERATIONS

We consider bandlimited white noise in the frequency range 1-2 GHz as our interrogating waveform. As our receiver is coherent, *i.e.*, it is a quadrature receiver, we may view this waveform as complex. It can be modeled as a stochastic voltage waveform $\mathcal{S}[t]$ that is zero mean, ergodic and possessing a power spectral density function

$$S(f) = \begin{cases} S_0, & f_0 - \beta/2 \le f \le f_0 + \beta/2 \\ 0, & \text{otherwise} \end{cases}, \tag{1}$$

where β is the bandwidth ($1\ GHz$), and f_0 is the mean frequency (1.5 GHz). The associated correlation function is given by

$$\begin{aligned} B(\tau) &= \int e^{2\pi j f \tau} S(f)\, df \\ &= E_0 e^{2\pi j f_0 \tau} \mathrm{sinc}(\beta\tau), \end{aligned} \tag{2}$$

where $E_0 = \beta S_0$ is the total power in the signal. This gives the system a down-range resolution of

$$\Delta x = c/2\beta = 15 \text{ cm}. \tag{3}$$

2.1. 1-DIMENSIONAL IMAGING

To aid in recalling what a coherent correlation receiver "sees" (such as the one shown in Fig. 1), we first examine the formation of 1-dimensional images, or range profiles. We transmit a random waveform and the received signal is mixed with a time delayed version of our transmitted waveform. After passing this through a low pass filter (and, in practice, an I/Q demodulator), the return signal is analyzed.

We will assume the "far-field weak scatter" model with nondispersive scatterers (see, for example, *Borden*[13]). Using this model, the random voltage waveform return of a target distribution function, $\rho(\tau)$, at the radar receiver is given by

$$\int \rho(\tau')\mathcal{S}[t-\tau']\, d\tau' + n(t), \tag{4}$$

where $n(t)$ is an additive noise process, and $\tau := 2R/c$ is the delay parameter associated with a target located at a range R. We assume that $n(t)$ is uncorrelated with our process $\mathcal{S}[t]$. Mixing this with $\mathcal{S}^*[t-\tau]$, for a fixed value of τ and sampling in time, yields

$$\mathcal{R}(t_m, \tau_n) := \int \rho(\tau')\mathcal{S}[t_m - \tau']\mathcal{S}^*[t_m - \tau_n]\, d\tau' + \mathcal{S}^*[t_m - \tau_n]n(t_m). \tag{5}$$

Taking the expectation of $\mathcal{R}$ yields the, not surprising, result

$$\hat{\rho}(\tau_n) := \mathbf{E}\{\mathcal{R}(t_m, \tau_n)\} = \int \rho(\tau')B(\tau_n - \tau')\, d\tau' = \rho \otimes B(\tau_n), \tag{6}$$

where the noise term decorrelates completely and $\otimes$ is the convolution operator. We see that the correlation function B plays the role of a 1-dimensional point-spread function.

Including the radar transfer function in this theoretical formulation has little effect on eqn. (6). Indeed, let $H(\nu)$ be the radar transfer function and $h(t)$ be the impulse response function. Also, recall the spectral representation[14] for (stationary) $\mathcal{S}[t]$

$$\mathcal{S}[t] = \int e^{2\pi j f t}\, dZ(f), \tag{7}$$

where equality is assumed in the *mean square sense*, and $Z(\nu)$ is a random interval function (a "random measure") with uncorrelated increments, *i.e.*

$$\mathbf{E}\{dZ(f)\ dZ^*(f')\} = \delta(f - f')S(f)df. \tag{8}$$

Substituting eqn. (7) into this into eqn. (5) yields

$$\mathcal{R}(t,\tau) \otimes h = \int \rho(\tau') \int\int e^{2\pi j f(\tau - \tau')} e^{2\pi j (f - f')t} H(f - f')dZ(f)dZ^*(f')\, d\tau' + (n(t)\mathcal{S}^*[t-\tau]) \otimes h. \tag{9}$$

Upon taking the expectation, we get a slightly altered definition of $\hat{\rho}$, namely,

$$\hat{\rho}(\tau) = H(0)(\rho \otimes B(\tau)). \tag{10}$$

In the ideal probabilistic sense, the radar only alters the image by the gain $H(0)$.

What we calculated in the previous paragraph is the theoretical expected image estimate. If one wished to perform a statistical analysis of our imaging system, one would also need to calculate the theoretical variance image. This is given by

$$\mathrm{Var}\{\mathcal{R}\} \;=\; \mathbf{E}\{\mathcal{R}^2(t,\tau)\} - \mathbf{E}\{\mathcal{R}(t,\tau)\}^2. \tag{11}$$

To calculate this variances we will make use of the following formula. Let X_1, X_2, X_3, and X_4 be zero mean normally distributed random variables. One can use the characteristic function of a family of normally distributed random variables to calculate

$$\mathbf{E}\{X_1X_2X_3X_4\} = \mathbf{E}\{X_1X_4\}\mathbf{E}\{X_2X_3\} + \mathbf{E}\{X_1X_3\}\mathbf{E}\{X_2X_4\} + \mathbf{E}\{X_1X_2\}\mathbf{E}\{X_3X_4\}. \tag{12}$$

In particular, if $\mathcal{S}[t]$ is real, *i.e.* when $\mathcal{S}[t] = \mathcal{S}^*[t]$, we have, on using eqn. (12), eqn. (2), and letting $X_i = \mathcal{S}[t_i]$,

$$\mathbf{E}\{\mathcal{S}[t_1]\mathcal{S}[t_2]\mathcal{S}[t_3]\mathcal{S}[t_4]\} = B(t_1 - t_4)B(t_2 - t_3) + B(t_1 - t_3)B(t_2 - t_4) + B(t_1 - t_2)B(t_3 - t_4). \tag{13}$$

So, under the assumption that $\mathcal{S}[t]$ is real valued . *i.e.* we only consider the inphase (I) and quadrature (Q) channels of our receiver separately, substituting eqn (13) into eqn (11) yields

$$\begin{aligned} \mathrm{Var}(\mathcal{R}) &= \mathbf{E}\{\mathcal{R}^2(t,\tau)\} - \mathbf{E}\{\mathcal{R}(t,\tau)\}^2 \\ &= (\rho \otimes B(\tau))^2 + B(0)\textstyle\int\int \rho(\tau')\rho(\tau'')B(\tau' - \tau'')\, d\tau' d\tau'' + B(0)\sigma_n^2, \end{aligned} \tag{14}$$

where σ_n^2 is the variance of the noise process $n(t)$. The first term above shows us that the variance is higher for those portions of the target with a high reflectivity. The second term characterizes how the sidelobes of B serve to blur the target. The last term is a direct consequence noise variance and the transmit signal variance.

Finally we point out that although formula (14) is useful in designing statistical tests for the estimate of $\hat{\rho}$, it is well know that if $s(t)$ is a realization of $\mathcal{S}[t]$ then

$$\langle s \rangle_T := \frac{1}{T}\int_0^T s(t)s^*(t+\tau)\, dt, \tag{15}$$

is an unbiased and consistent estimator of $B(\tau)$.[14]

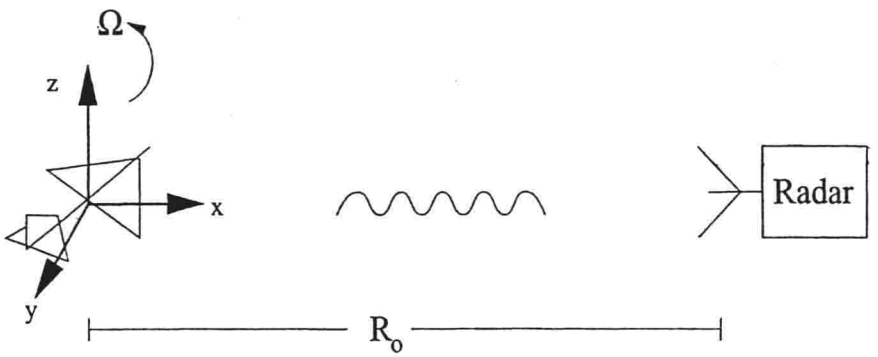

Figure 2. The geometry of inverse synthetic aperture radar.

2.2. 2-DIMENSIONAL IMAGING

We now discuss range-Doppler imaging, in particular ISAR imaging. However, much of what follows easily generalizes to SAR imaging. For a target rotating with axis of rotation transverse to the radar line of sight (LOS), we can define a natural target-centric coordinate system. For simplicity, we assume that the axis of rotation is perpendicular to the LOS. Let the LOS define the x-axis, the axis of rotation define the z-axis, and choose the y-axis to be perpendicular to these two directions, as seen from Fig. 2. Assume that the target is rotating at a constant angular velocity Ω and let R_0 be the distance between the radar antenna and the origin of our coordinate system. We, again, assume the far-field weak-scatterer model with nondispersive scatterers, and we denote $\rho(x, y$ as the target density function (the z-direction variation does not play any appreciable role in ISAR imaging[13]). The received waveform is then given by

$$r(t) = \int\int\int \rho(x, y, z)\mathcal{S}[t - \tau(x, y, t)]\, dxdydz, \tag{16}$$

where $\tau(x, y, t) = \frac{2(R_0 - x')}{c}$ with $x' = x\cos(\Omega t) + y\sin(\Omega t)$. Following the range-Doppler approach[16] to ISAR imaging, we make the approximation

$$\tau(x, y, t) \approx \frac{2(R_0 - x)}{c} + \frac{2\Omega y}{c}t = \tau(x) + \alpha(y)t. \tag{17}$$

This approximation transforms equation (16) into

$$r(t) \approx \int\int \rho(x, y)\mathcal{S}[(1 - \alpha(y))t - \tau(x)]\, dxdy. \tag{18}$$

Upon reception, $r(t)$ is mixed with a delayed replica of $\mathcal{S}[t]$, $\mathcal{S}^*[t - \tau_n]$, and sampled in time to yield

$$\mathcal{R}(t_m, \tau_n) = \int\int \rho(x, y)\mathcal{S}[(1 - \alpha(y))t_m - \tau(x)]\mathcal{S}^*[t_m - \tau_n)]\, dxdy \tag{19}$$

The desired measured data is the expectation of $\mathcal{R}(t_m, \tau_n)$ given by

$$\mathbf{E}\{\mathcal{R}(t_m, \tau_n)\} = \int\int \rho(x, y)B(\tau_n - \tau(x) - \alpha(y)t_m)\, dxdy. \tag{20}$$

The function $B(\tau_n - \tau(x) - \alpha(y)t_m)$ in equation (20) is the time domain point-spread function.

If the integration time T (the span of the time samples t_m) is small enough, then the rotation of the target will produce approximately constant Doppler frequencies for sub-scatterers in a particular range bin. We take the Fourier transform of $B(\tau_n - \tau(x) - \alpha(y)t_m)$ with respect to the variable t_m to obtain the frequency domain point-spread function

$$\hat{B}(\tau_n, y_m; \tau(x), \alpha(y)). \tag{21}$$

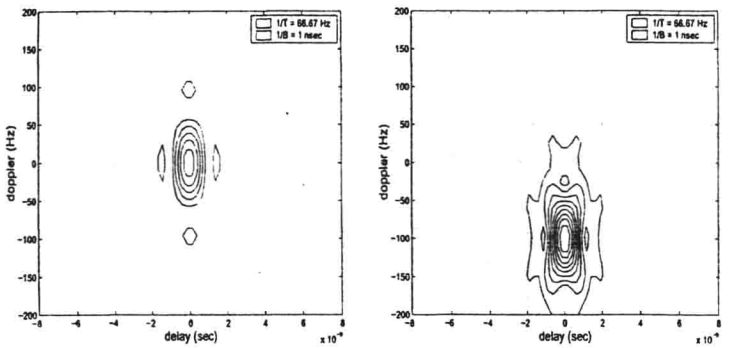

(a) Contour plot with no Doppler present.

(b) Contour plot with mean Doppler of 100 Hz.

Figure 3. The frequency domain point-spread function.

Table 1. Description of targets used.

Target	Description
A	Cylinders of radii 15 cm, and 33 cm.
B	Cube of dimensions 60×60×60 cm.
C	Corner reflector of side 35 cm.
D	Airplane shown in Fig. 4.

Using eqn. (2) we get

$$\hat{B}(\tau_n, y_m; \tau(x), \alpha(y)) = E_0 e^{2\pi j(\tau_n - \tau(x))\nu_0} \int_{-T/2}^{T/2} \mathrm{sinc}(\beta(\tau_n - \tau(x) - \alpha(y)t)) e^{-2\pi j(y_m - \alpha(y)f_0)t}\, dt \qquad (22)$$

As shown in *Bell et. al.*,[15] the modulus of this function is localized around the point $\tau_n = \tau(x)$, $y_m = \alpha(y)f_0$. The resolution in the τ-direction, *i.e.*, the down-range resolution, is proportional to $1/\beta$ and the resolution in the y-direction, *i.e.*, the cross-range resolution, is proportional to $1/T$ up to $O(\alpha^2)$. Fig. 3 shows the absolute value of the frequency domain point-spread function for the zero Doppler (stationary target) and the non-zero Doppler (moving target) cases. Using the fact that $\tau(x)$ and $\alpha(y)$ are proportional to the x and y coordinates, respectively, we arrive at our desired image.

3. EXPERIMENTAL RESULTS

To examine the effectiveness of an ultra-wideband random noise radar configured in ISAR mode, we conducted a series of turntable experiments. We use the radar system shown in figure 1. A full description of this system can be found in *Narayanan et. al.*.[4] To minimize background clutter, we collected data in an anechoic chamber, as shown in Fig. 5. Test targets were placed on a turntable of 1.2 m diameter. The top of the turntable was constructed of acrylic (dielectric constant of 3.3). This was placed on a wooden frame that housed an electric motor and motor control unit. The wooden frame was then covered with an microwave absorbing panel (Millimeter Wave Technology, Inc. MAC-6112) with relative absorption of about −19 dB over 1-2 GHz.

We used several test targets in our experiments. These are listed in the Table 1. Target A consisted of two metallic cylinders of diameters 15 cm and 33 cm, respectively. Target B was a 60×60×60 cm cube with its center placed on the turntable's axis of rotation, constructed of cardboard and covered with aluminum foil. This target possesses both co-polarized (the flat faces) and cross-polarized (the edges) scattering characteristics. Target C was a 35 cm corner reflector with its apex placed slightly off of the turntable's axis of rotation. The final target, Target D, was a model plane, as shown in Fig. 4. It fuselage was constructed of an aluminum conduit, and its wings were

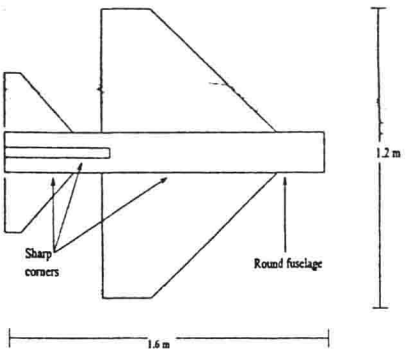

Figure 4. The model plane (Target D).

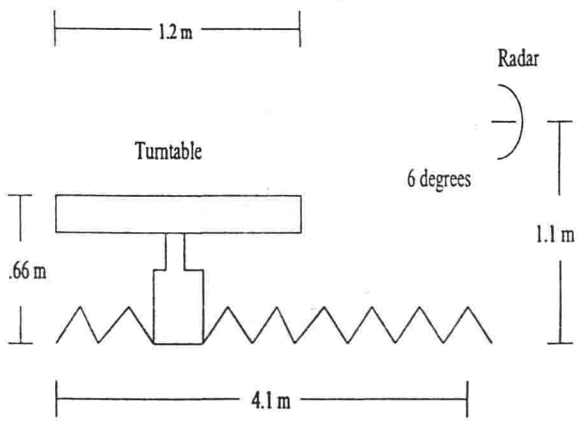

Figure 5. Geometry of the experimental setup.

made of cardboard covered with aluminum foil. All of the targets were placed directly on the turntable (as shown in Fig. 5) except for the plane, which was elevated on cardboard pylons to create a grazing angle of 14°. Finally, a technique was deviesed to simulate the collection in all range bins simultaneously.

3.1. Cross-Range Resolution

If our system were a narrow band system, then the cross range resolution, Δy, would be given approximately by[16]

$$\Delta y = \frac{\lambda}{2\Delta\theta}, \tag{23}$$

where λ is the wavelength of the carrier frequency, or mean wavelength, and $\Delta\theta$ is the rotation angle over which the measurement is made ($\Delta\theta$ is usually a small angle). However, since the fractional bandwidth of our system was 2/3, the narrow band approximation may or may not be valid. The main lobe of the point spread function, as seen in Fig. 3 and discussed in *Bell et. al.*,[15] localized around the location of a point scatterer, and, as stated in the previous

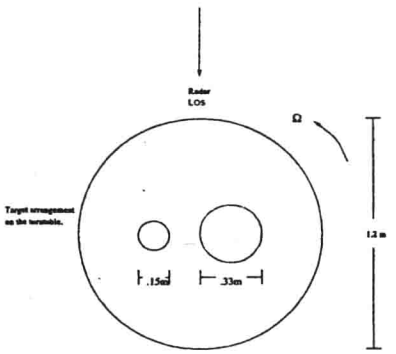

(a) Target arrangement for the cross-range resolution experiment.

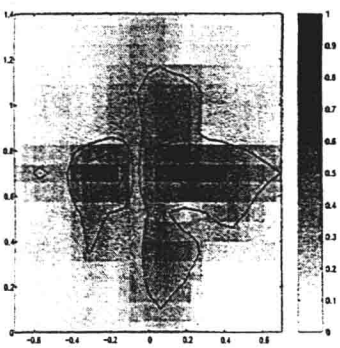

(b) Narrowband predicted cross-range resolution of 15 cm (normalized returns).

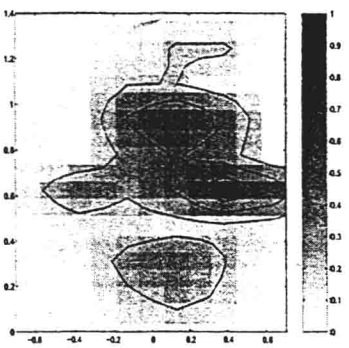

(c) Narrowband predicted cross-range resolution of 30 cm (normalized returns).

Figure 6. The cross-range resolution experimental setup and results.

section, is of width $1/T$ up to order $O(\alpha^2)$. To examine whether one can use eqn. (23) effectively, we conducted an experiment involving the two cylinders (Target A) described in the previous section. The target arrangement is shown in Fig. 6(a). Using the mean wavelength of 20 cm, eqn. (23) predicts a cross-range resolution of 15 cm (giving a square resolution window) for $\Delta\theta \approx 20°$, and a cross-range resolution of 30 cm for $\Delta\theta \approx 40°$. We point out that our L-band radar is not well suited for these experiments, owing to its large wavelength, since in order to achieve cross-range resolution on the same scale as down-range resolution, we need to rotate through large angles. This will result in image blurring due to range walk phenomenon. Despite this difficulty, the ISAR images for these two values of $\Delta\theta$ shown in Fig. 6(b) and 6(c), demonstrate that we do achieve a cross-range resolution on the order of that predicted by eqn. (23). Indeed, we can see that the smaller cylinder is distinguishable from the larger cylinder when $\Delta\theta \approx 40°$, but the two are much harder to distinguish when $\Delta\theta \approx 20°$, as predicted by equation (23). In what follows, we will use this relationship to place cross-range scales on all our displayed images.

3.2. Variation from Look to Look

Each image that one obtains with a random signal radar is a single realization, or look, of a random field. Single look images of the corner and side of a the cube are shown in Fig. 7. Not only is there variation from ambient noise both in the environment and the hardware, but there is also natural variation from the fact that the noise signal does